

## RESEARCH ARTICLE

10.1002/2015JA021803

## Key Points:

- Empirical models of hiss as a function  $Kp$ ,  $L$ , latitude, and MLT are presented
- Comparison between hiss measurements on Van Allen Probes and CRRES performed
- No saturation of amplitude with  $Kp$ , no latitudinal dependence, MLT dependence symmetric about noon

## Supporting Information:

- Text S1, Equation S1, and Caption for Table S1
- Table S1

## Correspondence to:

M. Spasojevic,  
mariaspasojevic@stanford.edu

## Citation:

Spasojevic, M., Y. Y. Shprits, and K. Orlova (2015), Global empirical models of plasmaspheric hiss using Van Allen Probes, *J. Geophys. Res. Space Physics*, 120, 10,370–10,383, doi:10.1002/2015JA021803.

Received 12 AUG 2015

Accepted 14 NOV 2015

Accepted article online 18 NOV 2015

Published online 11 DEC 2015

## Global empirical models of plasmaspheric hiss using Van Allen Probes

M. Spasojevic<sup>1</sup>, Y. Y. Shprits<sup>2,3</sup>, and K. Orlova<sup>4</sup>
<sup>1</sup>Department of Electrical Engineering, Stanford University, Stanford, California, USA, <sup>2</sup>Department of Earth, Planetary, and Space Sciences, University of California, Los Angeles, California, USA, <sup>3</sup>Department of Earth, Atmospheric and Planetary Sciences, Massachusetts Institute of Technology, Cambridge, Massachusetts, USA, <sup>4</sup>Skolkovo Institute of Science and Technology, Moscow, Russia

**Abstract** Plasmaspheric hiss is a whistler-mode emission that permeates the Earth's plasmasphere and is a significant driver of energetic electron losses through cyclotron resonant pitch angle scattering. The Electric and Magnetic Field Instrument Suite and Integrated Science instrument on the Van Allen Probes mission provides vastly improved measurements of the hiss wave environment including continuous measurements of the wave magnetic field cross-spectral matrix and enhanced low-frequency coverage. Here, we develop empirical models of hiss wave intensity using two years of Van Allen Probes data. First, we describe the construction of the hiss database. Then, we compare the hiss spectral distribution and integrated wave amplitude obtained from Van Allen Probes to those previously extracted from the Combined Release and Radiation Effects Satellite mission. Next, we develop a cubic regression model of the average hiss magnetic field intensity as a function of  $Kp$ ,  $L$ , magnetic latitude, and magnetic local time. We use the full regression model to explore general trends in the data and use insights from the model to develop a simplified model of wave intensity for straightforward inclusion in quasi-linear diffusion calculations of electron scattering rates.

## 1. Introduction

Plasmaspheric hiss is an unstructured, extremely low frequency whistler-mode radio emission that permeates the high-density region in the Earth's inner magnetosphere [Hayakawa and Sazhin, 1992; Bortnik et al., 2009, and references therein]. The energy source for the waves may have contributions from chorus emissions [Bortnik et al., 2008, 2011] and lightning-generated whistlers [Sonwalkar and Inan, 1989; Green et al., 2005; Meredith et al., 2006a], and this wave energy can be further amplified by anisotropic electron distributions in the few to hundred keV energy range [Thorne et al., 1979; Chen et al., 2012a]. Through cyclotron resonant pitch angle scattering, plasmaspheric hiss is a major driver of radiation belt electron losses [Millan and Thorne, 2007; Shprits et al., 2008, and references therein] and may be the dominant loss mechanism within the slot region [Lyons and Thorne, 1972, 1973; Abel and Thorne, 1998; Meredith et al., 2007] as well as in the outer belt following geomagnetic storms [Meredith et al., 2006b; Lam et al., 2007; Shprits et al., 2009, 2013; Thorne et al., 2013].

Electron pitch angle scattering rates and resulting electron lifetimes have traditionally been computed using quasi-linear diffusion theory and have been shown to be in reasonable agreement with satellite observations [Abel and Thorne, 1998; Albert, 2000; Selesnick et al., 2003; Meredith et al., 2006b, 2007, 2009]. However, accurate estimation of electron lifetimes requires accurate models of the global wave environment including models of time-averaged wave magnetic field intensity, spectral distribution, and wave normal distribution as a function of position and geomagnetic activity. Wave data from the Combined Release and Radiation Effects Satellite (CRRES) have been used extensively in studies of the global distribution of hiss and the resulting impact on electron lifetimes. Notably, Meredith et al. [2004] produced global maps of hiss intensity, and Orlova et al. [2014] provided empirical fits as a function of  $Kp$ ,  $L$ , and  $\lambda$  for dayside and nightside hiss using CRRES data. However, the CRRES plasma wave instrument consisted of only a single-channel electric field measurement, and a number of assumptions must be used to process the data. Agapitov et al. [2014] recently used data from the Akebono spacecraft to parametrize hiss at lower  $L$  ( $L < 2$ ) than was available from CRRES. Data from the Time History of Events and Macroscale Interactions during Substorms spacecraft have been used to create

global models of hiss with both *Golden et al.* [2012] and *Kim et al.* [2015] examining the role of the time history of the solar wind on hiss wave amplitudes. Analysis of Cluster data has provided new insights on the wave normal distribution of hiss [Agapitov et al., 2013], and measurements by both Cluster [Agapitov et al., 2013] and Polar [Tsurutani et al., 2015] show that hiss is widely distributed in magnetic latitude extending to  $\lambda > 45^\circ$ .

The Van Allen Probes mission was designed to study the processes that drive the dynamics of the radiation belts and has unprecedented coverage of the magnetospheric wave environment [Mauk et al., 2012]. Electric and Magnetic Field Instrument Suite and Integrated Science (EMFISIS) [Kletzing et al., 2013] provides vastly improved measurements of plasmaspheric hiss including continuous measurements of the wave electric and magnetic field cross-spectral matrix and enhanced low-frequency coverage. Using Van Allen Probes data, *Li et al.* [2015] presented maps of hiss wave magnetic field amplitude as a function of  $L$  and magnetic local time (MLT) for three levels of magnetic activity: quiet ( $AL^* \geq 100$  nT), moderately disturbed ( $500 \leq AL^* < 100$  nT), and active ( $AL^* < 500$  nT) where  $AL^*$  is the minimum value of  $AL$  index in the previous 3 h. *Li et al.* [2015] also closely examined the spectral distribution of hiss and presented new non-Gaussian parameterizations, which extend to lower frequency and provide a better fit to the asymmetric hiss frequency distribution than conventional frequency models.

The current study analyzes a database of hiss observations from Van Allen Probes and complements the work of *Li et al.* [2015]. In section 2, we describe the construction of the 2 year hiss database using data from one of the Van Allen Probes, Radiation Belt Storm Probe A (RBSP A). In section 3, we perform detailed comparisons of the hiss spectral distribution and integrated wave amplitude obtained from RBSP A to that previously extracted from CRRES. In section 4, we develop a cubic regression model of the average hiss magnetic field intensity as a function of  $Kp$ ,  $L$ ,  $\lambda$ , and MLT. We use the full regression model to explore general trends in the data and use insights from the model to develop a simplified model of wave intensity, presented in section 5, for straightforward inclusion in quasi-linear diffusion calculations of electron scattering rates. A key advantage of the second model is the parametrization of hiss intensity to higher values of  $Kp$ , which can be applied to modeling the dynamics of electrons during geomagnetic storms.

## 2. Hiss From RBSP A Data

In order to extract the plasmaspheric hiss wave amplitude and spectral distribution, we use data from the EMFISIS instrument on the RBSP A spacecraft from 1 October 2012 to 30 September 2014 (orbits 86–2035). Figure 1 shows an example of the procedure for the inbound portion of orbit 128 from 17 October 2012. The first step is to identify intervals when the spacecraft is inside the plasmasphere. For this we use the EMFISIS Level 2 High Frequency Receiver (HFR) spectra, which provides a single-channel electric power spectral density in the range of 10 to 487 kHz with 6 s time resolution (Figure 1a). Plasmapause boundary crossings are manually identified for each orbit. We use the upper hybrid resonance (UHR) band [Mosier et al., 1973] to identify sharp density gradients in the plasma. The UHR band is often the most intense feature in the HFR spectra and can be robustly used to determine the electron plasma density [Kurth et al., 2015]. Multiple inbound and outbound plasmapause crossing can be selected on a given orbit, allowing us to capture features such as plasmaspheric plumes. For orbits when the density gradually changes with  $L$ , we make a best estimate of the boundary separating low- and high-density plasma using features such as disappearance of the  $n + 1/2$  electron cyclotron harmonics in the high-density region and distinct changes in the nature of the wave spectrum below 10 kHz (using the EMFISIS Waveform Receiver (WFR), discussed below). On about 35% of orbits, the spacecraft appears to remain within the plasmasphere for the entire orbit. The vertical white line in Figure 1a shows the location of the plasmapause at  $L = 4.2$  on the inbound segment of orbit 128.

The plasmaspheric hiss wave amplitude and spectra are extracted using the EMFISIS Level 2 Waveform Receiver (WFR) data, which provides the diagonal elements of the electric and magnetic cross-spectral matrix ( $B_u B_u$ ,  $B_v B_v$ ,  $B_w B_w$ ,  $E_u E_u$ ,  $E_v E_v$ , and  $E_w E_w$ ) as defined in the UVW spacecraft coordinate system (where the UV plane is the spacecraft spin plane and W is along spin axis) [Kletzing et al., 2013] from 2 Hz to 11.2 kHz with 6 s time resolution. Figure 1b shows the WFR  $B_u B_u$  component for a segment of orbit 128. Outside the plasmapause (to the left of the vertical white line), banded chorus emissions can be seen just below half the local gyrofrequency (yellow line in Figures 1a and 1b) in the range of a few kilohertz, increasing in frequency with decreasing  $L$ . Inside the plasmapause, plasmaspheric hiss can be seen extending from about 100 Hz to a few kilohertz. By examining the larger data set, we have identified the hiss band as extending from 40 Hz to 2 kHz (indicated by the horizontal magenta lines in Figure 1b). However, at the low  $L$  values near perigee,

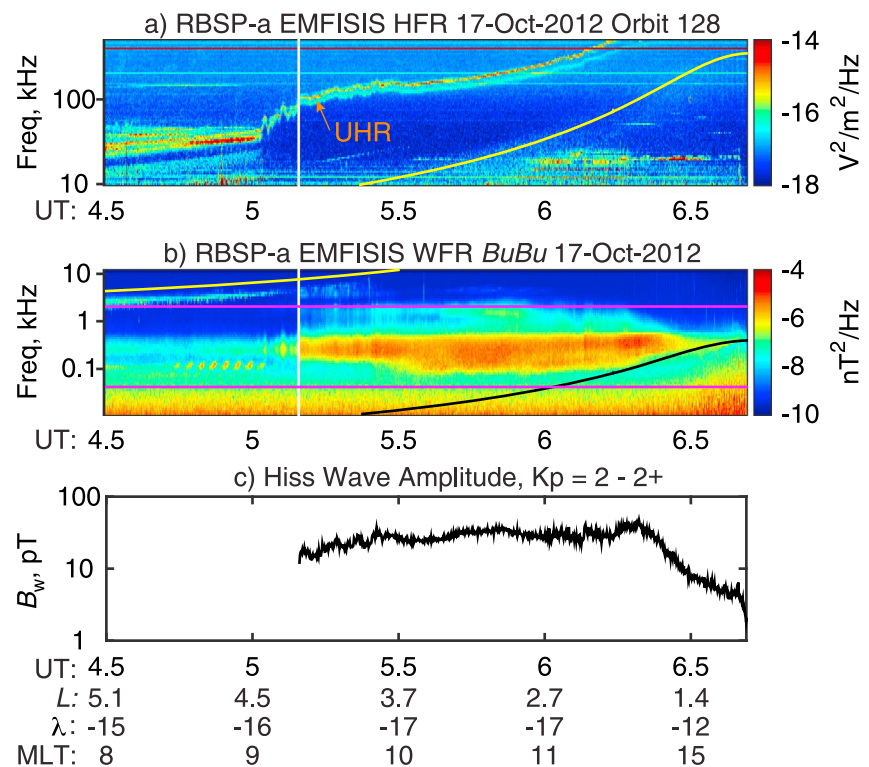


**Figure 1.** (a) RBSP A EMFISIS HFR data for portion of the inbound pass of orbit 128 on 12 October 2012 showing the distinct upper hybrid resonance (UHR) line, and the manually selected location of the plasmapause is indicated with the vertical white line. The yellow curve is one-half the local gyrofrequency. The plot extends from 10 kHz to 487 kHz with a log frequency scale. The color scale indicates the power spectral density on a log scale. (b) EMFISIS WFR  $B_u B_u$  component of the cross-spectral matrix showing observations of plasmasphere hiss. The yellow line is one-half of the local electron gyrofrequency, and the black line is the proton cyclotron frequency. The horizontal magenta lines are at 40 Hz and 2000 Hz and indicate the hiss band. The plot extends from 10.7 Hz to 11.2 kHz with a log frequency scale. (c) The total hiss wave magnetic field amplitude for this interval.

ion cyclotron noise extends into this band with upper boundary likely near the two-ion cutoff [Gurnett and Burns, 1968; Smith and Brice, 1964]. Therefore, to obtain the hiss wave magnetic field amplitude ( $B_w$ ), we add the diagonal components of the spectral matrix ( $B_u B_u$ ,  $B_v B_v$ , and  $B_w B_w$ ) and integrate the power spectral density (PSD) from the larger of 40 Hz or the proton cyclotron frequency (black line in Figure 1b) up to 2 kHz and take the square root of that value. Figure 1c shows that for this weakly disturbed interval ( $K_p = 2 - 2+$ ), the hiss wave amplitudes are in the range of 15–45 pT. Similarly, to obtain the hiss wave electric field amplitude, we use the  $E_u E_u$  and  $E_v E_v$  components of the cross-spectral matrix. The  $E_w E_w$  component is not used since it is contaminated by periodic impulses due to shadowing of the spin plane electric field boom [Wygant et al., 2013]. Further, to obtain the wave electric field amplitude, the spectral densities are integrated up to 1.9 kHz since there is a fairly persistent interference line at 2 kHz in the WFR electric field data. The hiss electric and magnetic spectral density profiles and wave amplitudes are tabulated for all orbits from 86 to 2035 with the exception of orbits 543 to 548 where the WFR instrument appears to have a gain/mode change. The RBSP A hiss database created in this analysis has 7.5 million measurements of hiss wave amplitude and spectral distribution.

### 3. Comparison With CRRES Data

Prior to the launch of the Van Allen Probes spacecraft, a widely used source of data on plasmaspheric hiss has been the CRRES plasma wave experiment [Anderson et al., 1992], which operated in 1990–1991. Although the orbit of the CRRES spacecraft was well suited for studies of the radiation belts and the mission operated during a period of solar maximum, the plasma wave experiment itself had extremely limited capabilities. Since a large number of studies on radiation belt dynamics have utilized CRRES plasma wave measurements

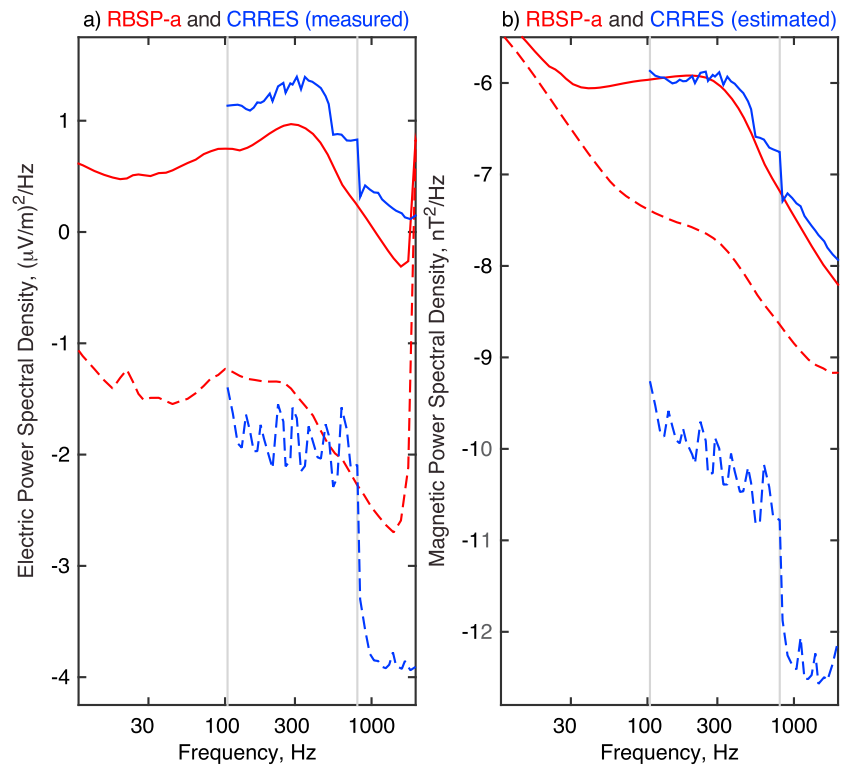


**Figure 2.** (a) The electric field power spectral density on a log scale measured by RBSP A (red) and CRRES (blue). (b) The magnetic field power spectral density on a log scale measured by RBSP A (red) and inferred from electric field measurements on CRRES (blue). In Figures 2a and 2b, the averages are performed using data in the range  $2.5 < L < 5.5$ . The dashed curves are averages of the lowest 1% quantile of data (based on total power integrated from 0 to 1.9 kHz) and provide an estimate of the instrument noise floor. The solid curves are averages of the 1% to 95% quantile of data. The vertical gray lines show the interfaces between the CRRES SFR bands.

[e.g., Li *et al.*, 2007; Summers *et al.*, 2007; Lam *et al.*, 2007; Meredith *et al.*, 2007, 2009; Orlova *et al.*, 2014], it is important to compare the wave data from CRRES to the newer Van Allen Probes measurements.

The CRRES plasma wave experiment consisted of a single-channel electric field measurement. However, quasi-linear energy and pitch angle scattering rates scale as the square of wave magnetic field amplitude [Kennel and Engelmann, 1966]. Therefore, to apply CRRES measurements to calculate electron scattering rates, the measured electric power spectral densities are converted to magnetic power spectral densities using the whistler-mode dispersion relation assuming parallel propagation. This  $E$  to  $B$  conversion was first done by Meredith *et al.* [2004], and all subsequent studies of hiss-driven diffusion using CRRES data, such as cited above, use the inferred wave magnetic field intensity. Therefore, we perform two types of comparisons between CRRES and RBSP A. First, we compare the measured CRRES electric field to the measured RBSP A electric field, and then we compared the inferred CRRES magnetic field to the measured RBSP A magnetic field.

We use a database of hiss wave amplitude and spectra from CRRES which was compiled by Orlova *et al.* [2014] but used essentially the same procedure as Meredith *et al.* [2004]. Full details of the methodology can be found in those publications, but we highlight a few aspects of the CRRES data for comparison with Van Allen Probes. Hiss amplitudes on CRRES are inferred from the sweep frequency receiver (SFR) driven by a single-channel electric field antenna oriented in the ecliptic plane. In order to convert the electric PSD to magnetic PSD, it is assumed that the waves are propagating parallel to the geomagnetic field,  $B_0$ . The electric PSD is spin averaged and multiplied by two, and this quantity is assumed to be the total wave electric PSD oriented perpendicular to the direction of  $B_0$ . The electric PSD is converted to magnetic PSD using the whistler-mode dispersion relation and ancillary measurements of  $B_0$  from the magnetometer [Singer *et al.*, 1992] and electron density derived from the UHR band [Ledocq *et al.*, 1994]. In contrast, the EMFISIS instrument directly measures all three components of the magnetic PSD.

Figure 2a shows comparisons of the average electric power spectral density as a function of frequency measured by RBSP A (red) and CRRES (blue). The dashed lines are the averaged spectra for the quietest 1% of measurements (as calculated by the total integrated power from 0 to 1.9 kHz) inside the plasmasphere and in the range of  $2.5 < L < 5.5$ . These curves are taken as an estimate of the noise floor of the instrument. The lowest frequency measured by CRRES is 100 Hz while RBSP A extends down to 2 Hz. Also, there is distinct break in the CRRES spectrum at 800 Hz that corresponds to the interface between the SFR band 1 (100–800 Hz with  $\Delta f = 7$  Hz) and band 2 (800 Hz–6.4 kHz with  $\Delta f = 56$  Hz). The jump in the PSD at 800 Hz suggests there may be an issue with the calibration of the CRRES electric field. Within each band, the CRRES noise floor is irregular, possibly indicating interference from other spacecraft systems. In contrast, the RBSP A noise floor (dashed red) is fairly smooth with the exception of the 2 kHz interference line mentioned previously.

The solid lines in Figure 2a are the averaged spectra for the 1 to 95% quantile of measurements from inside the plasmasphere and in the range of  $2.5 < L < 5.5$ . In both data sets, we see a broad peak centered near 300 Hz that corresponds to plasmaspheric hiss. In the CRRES spectrum (solid blue line), the discontinuity near 800 Hz is still present, and the spectrum is noisier compared with RBSP A (solid red line). Further, the CRRES electric PSD is consistently about half an order of magnitude higher than RBSP A.

Next, Figure 2b shows comparisons of the average magnetic power spectral density measured by RBSP A (red) and inferred from CRRES (blue). First of all, we notice that the CRRES noise floor (dashed blue line) is now at least 2 orders of magnitude lower than RBSP A (dashed red). This is simply due the fact that electric field instruments generally have significantly higher sensitivity than magnetic field instruments, and thus the inferred CRRES  $B$  field extends to lower values than can be measured by an actual  $B$  field instrument. In the averaged spectra for the 1 to 95% quantile (solid lines), the inferred CRRES magnetic PSD tends to be higher than RBSP A, although the difference is less pronounced than in the electric field comparison.

The RBSP A magnetic field data indicate that the average spectrum of hiss extends to lower frequency with local minimum near about 40 Hz. The observed lower frequency extent of hiss (first reported by *Li et al.* [2013]) is important since previous attempts to model the effects of hiss on energetic electron lifetimes have generally used a lower cutoff of 100 Hz. The wave frequency distribution is critical in determining the resonant electron energies, with lower frequency waves interacting with higher-energy electrons.

Overall, we find that the RBSP A wave receivers have a smooth frequency response in the hiss frequency band with the exception of a persistent but narrow band interference line at 2 kHz in the electric field instrument. In contrast, the CRRES data are noisier, and a significant discontinuity in the spectral density profile occurs at the interface between the SFR band 1 and band 2, suggesting an issue with the instrument calibration. The CRRES lower frequency bound is 100 Hz, and the RBSP A data show that there is significant hiss wave power below that frequency.

Next, we compare the hiss wave amplitudes extracted from the two data sets, but first it is important to understand differences in the sampling distribution of the measurements. Figure 3 shows the probability distribution of hiss measurements as function of (a)  $Kp$ , (b)  $L$ , (c) magnetic latitude ( $\lambda$ ), and (d) magnetic local time (MLT) for CRRES in blue and RBSP A in red. Although both missions operated during the solar maximum, solar cycle 22 during CRRES operations was significantly more intense than solar cycle 24 of Van Allen Probes. The median  $Kp$  for the hiss data collected by CRRES is 2, and 11% of measurements have  $Kp > 4$ . For RBSP A, the median  $Kp$  for the hiss intervals is 1, and only 2% have  $Kp > 4$ . In terms of the  $L$  distribution of measurements (Figure 3b), the apogee of CRRES was slightly higher than RBSP A allowing for more measurements at higher  $L$ . However, hiss measurements on CRRES fall off rapidly below  $L = 2.5$ . This is due to the fact that the cold plasma density is used in the  $E$  to  $B$  conversion performed on the CRRES data. The CRRES SFR had a maximum frequency of 400 kHz allowing for density measurements as extracted from the UHR line up to about  $2000 \text{ cm}^{-3}$ , and thus limiting  $E$  to  $B$  conversion to the higher  $L$  values. In terms of magnetic latitude (Figure 3c), the RBSP A measurements are more concentrated at the equator and fall off rapidly for  $|\lambda| > 18^\circ$  while CRRES extends to higher latitudes. Finally, exactly 2 years of RBSP A data have been analyzed such that the MLT coverage is flat (Figure 3d), whereas the CRRES data have significant coverage gaps in the prenoon sector.

In Figure 4, we compare the integrated wave amplitude inside the plasmasphere in the hiss frequency band between CRRES (blue) and RBSP A (red). Figure 4a shows the probability distribution of all values of  $E_w$  calculated by integrating the measured electric PSD from 0.1 to 1.9 kHz. There are spikes in the distributions at low amplitudes (particularly in the CRRES data) likely due to noise or interference issues. Figure 4b shows



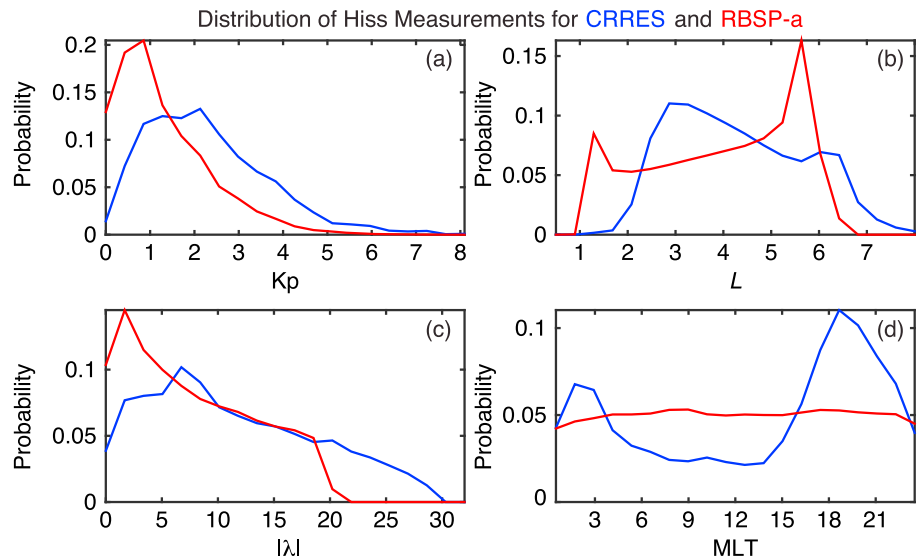


**Figure 3.** The probability distribution of hiss measurements for RBSP A (red) and CRRES (blue) as a function of (a)  $K_p$ , (b)  $L$ , (c) magnetic latitude, and (d) magnetic local time.

the distributions of all values of  $B_w$  calculated by integrating the inferred CRRES and measured RBSP A magnetic PSD from 0.1 to 2.0 kHz. There is a strong peak in the distribution for RBSP A near 1 pT, while the CRRES data extend to much smaller values of  $B_w$ . This is due to the difference in the noise floors as discussed earlier in association with Figure 2b. Figures 4c and 4d compare the amplitude probability distributions above a threshold value of 10  $\mu\text{V/m}$  in the electric field and 1.5 pT in the magnetic field. The CRRES distributions are shifted to significantly higher amplitude with the mean value (dashed lines) of  $E_w$  being 1.65 times higher and  $B_w$  being 1.44 times higher than RBSP A. These differences are significant particularly when recognizing that the electron scattering rates scale with  $\langle B_w^2 \rangle$ .

In Figures 4e and 4f, we further constrain the amplitudes to look only in the range of  $1 \leq K_p \leq 2.5$  and find that there is improved agreement between the distributions. However, constraining the data in the other dimensions is also important, and in Figures 4g and 4h, we select broad region of maximal overlap further limiting the data to middle  $L$  values ( $2.5 \leq L \leq 5.5$ ), lower latitude ( $0 \leq |\lambda| \leq 18$ ), and nightside ( $6 > \text{MLT} \geq 18$ ) measurements. The discrepancy in the  $\langle E_w \rangle$  is reduced, and the mean value of CRRES is only 1.16 times larger than RBSP A. For  $\langle B_w \rangle$ , CRRES is 1.3 times larger than RBSP A, and further  $\langle B_w^2 \rangle$  is 2 times larger.

In addition to differences in the constrained average amplitude of the CRRES and RBSP A data sets, we also find differences in the functional dependence of amplitude, particularly on magnetic latitude. In Figure 5a, the same constraints on  $K_p$ ,  $L$ , and MLT are applied as in Figure 4g, and we plot  $\langle E_w \rangle$  as a function of  $|\lambda|$ . The amplitudes are averaged in 12 quantiles of latitude resulting in different latitudes for the bin centers between the two spacecraft. CRRES (blue) observes a peak in amplitude near the equator and a minimum near  $5^\circ$  with amplitude increasing with latitude above  $5^\circ$ . RBSP A observes a somewhat similar trend, although the peak near the equator is less pronounced. The peak near the equator may be the result of electrostatic emissions that are confined to narrow-latitude range about magnetic equator.

When the CRRES inferred values of  $\langle B_w \rangle$  are used (Figure 5b), the trend from  $\langle E_w \rangle$  is mimicked with local maximums at the equator and higher latitude with a broad minimum in wave amplitude from 5 to  $15^\circ$ . This trend in CRRES  $\langle B_w \rangle$  was previously reported in analysis by Meredith *et al.* [2004, Figure 5] and Orlova *et al.* [2014, Figure 1]. On the other hand, for RBSP A, we see that hiss  $\langle B_w \rangle$  is fairly constant with latitude, and we do not see any indication of intense equatorially confined emissions or an increase in amplitude at higher latitudes.

With the caveat that CRRES has more limited coverage on the dayside, the MLT constraint is changed to  $6 \leq \text{MLT} < 18$  in Figures 5c and 5d. For  $\langle E_w \rangle$  (Figure 5c), RBSP A does not observe a local maximum at the equator but does follow the trend of increasing  $\langle E_w \rangle$  with latitude above about  $10^\circ$ . When examining the inferred values of  $\langle B_w \rangle$  on the dayside (Figure 5d), CRRES has a convex dependence with latitude and a very large

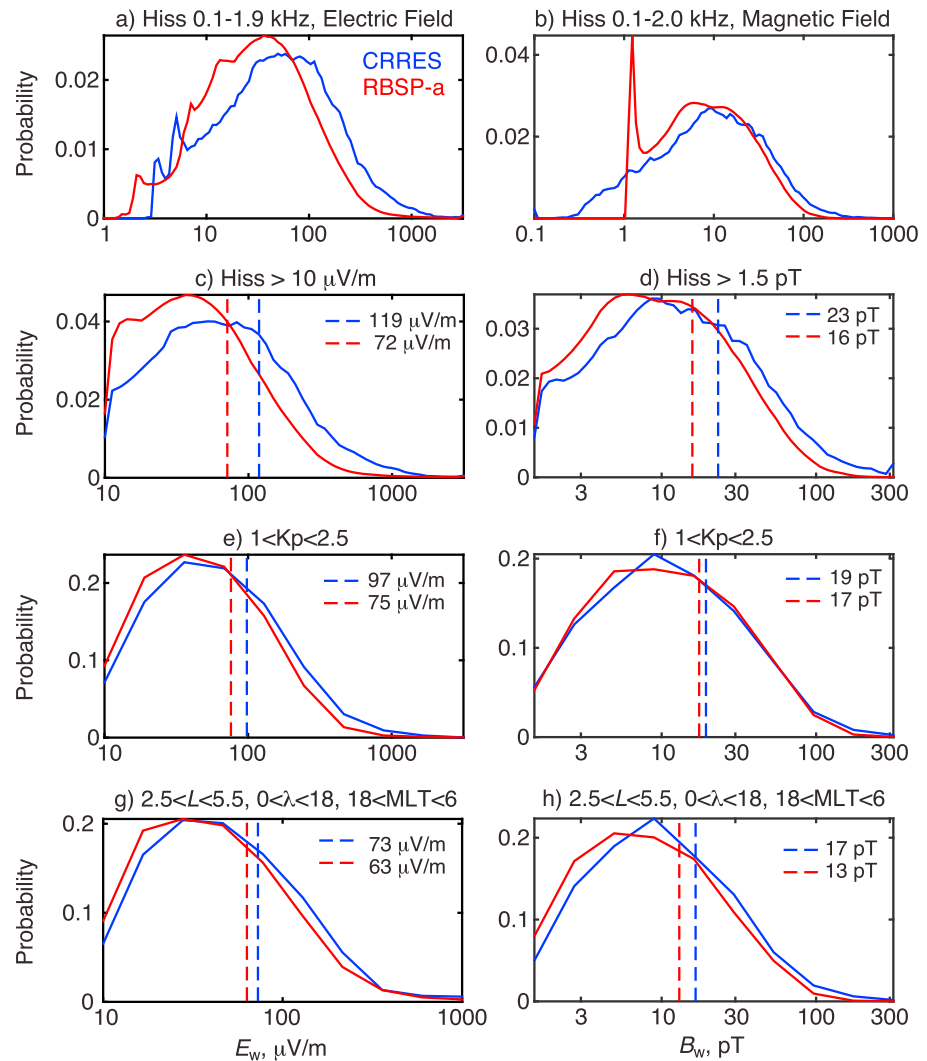


**Figure 4.** Comparisons of integrated wave amplitude in the plasmasphere between CRRES (blue) and RBSP A (red). The dashed lines indicate the mean value of the distributions. The probability distribution as integrated from (a) 100 Hz to 1.9 kHz in the electric field and (b) 100 Hz to 2.0 kHz in the magnetic field. The distributions above a threshold value of (c)  $E_w > 10 \mu\text{V/m}$  and (d)  $B_w > 1.5 \text{ pT}$ . (e and f) The distributions are above the threshold and further constrained by  $K_p$ . (g and h) The distributions are above the threshold and constrained by  $K_p$ ,  $L$ ,  $\lambda$ , and MLT.

average amplitude at the highest latitude quantile. In contrast, the measured values of  $\langle B_w \rangle$  from RBSP A are flat with latitude on the dayside similar to the nightside profile.

In summary, when comparing  $\langle E_w \rangle$  from CRRES and RBSP A, we find that agreement between the measured amplitude distributions is reasonably good when the data are properly constrained by  $K_p$ ,  $L$ ,  $\lambda$ , and MLT. CRRES does still tend to have more high amplitude measurements (as seen in Figure 4g), and this may be attributed to (1) assumptions made when estimating total wave amplitude from single-channel electric field measurements or (2) issues with CRRES instrument calibration as indicated by the discontinuity in the electric power spectral density at 800 Hz. Also, when examining  $\langle E_w \rangle$  as a function of latitude, CRRES observes a peak near the equator that is not as apparent in the RBSP A data (Figures 5a and 5c).

On the other hand, there is a larger difference between the constrained average amplitudes when comparing  $\langle B_w \rangle$  (Figure 4h). Further, the striking difference in the functional dependence of  $\langle B_w \rangle$  with latitude between CRRES and RBSP A calls into question the assumptions used in the CRRES  $E$  to  $B$  conversion. Recent observations of the hiss wave normal distribution suggest that the waves may be field aligned near the equator but become more oblique with increasing latitude [Agapitov *et al.*, 2013]. Thus, the parallel propagation

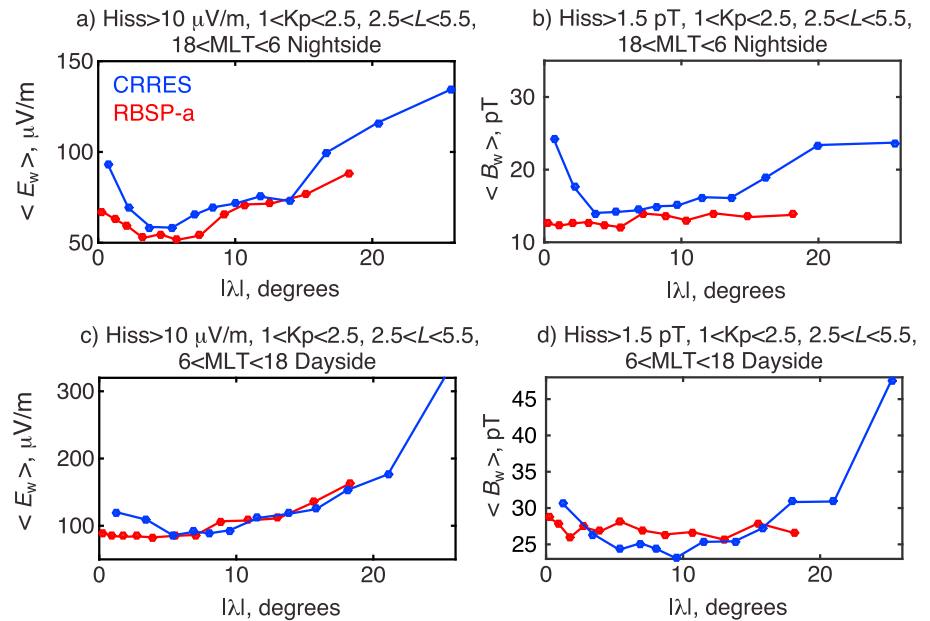


**Figure 5.** Average hiss amplitude as a function of magnetic latitude on the nightside and further constrained by  $K_p$  and  $L$  for the (a) electric field and (b) magnetic field for CRRES (blue) and RBSP A (red). Same on the dayside for (c) electric field and (d) magnetic field.

assumption in the  $E$  to  $B$  conversion would result in an overestimate of the wave amplitude (as was also discussed in Ni *et al.* [2011]), and this may be the effect we are seeing in CRRES  $\langle B_w \rangle$  at latitudes above  $15^\circ$ .

When initially undertaking this study, we had hoped that it would be possible to combine the CRRES and RBSP A data sets in order to construct a more comprehensive empirical model of plasmaspheric hiss. In particular, the CRRES data provide enhanced coverage to higher values of both  $K_p$  and  $\lambda$ . However, the differences in the constrained average amplitude (Figure 4h) and the functional dependence of amplitude with latitude (Figures 5b and 5d) between CRRES and RBSP A suggest it may be better to move away from the CRRES data and construct a new model solely based on the high-confidence measurements from RBSP A.

#### 4. Regression Model of Hiss Intensity

Next, we develop empirical models for the average hiss magnetic field intensity,  $\langle B_w^2 \rangle$ , as a function of  $K_p$ ,  $L$ ,  $\lambda$ , and MLT. In this section, we develop a multiple regression model using all four input variables. We provide the coefficients for the model and use the output of the model to explore general trends in the data. Then in the next section, we use insights from the regression model to develop a simplified model of  $\langle B_w^2 \rangle$ .

To construct the regression model, we take the all measurements inside the plasmopause in the range of  $1.5 < L < 5.5$ . The value of  $K_p$  is linearly interpolated to each data point. As discussed in Orlova *et al.* [2014], creating a wave model appropriate for use in calculating diffusion coefficients requires the data to be binned and averaged prior to performing the regression analysis. Thus, we divide the data into 12.5% quantile bins in  $K_p$ ,  $L$ ,  $\lambda$ , and MLT and compute the average value of  $B_w^2$  in this  $8 \times 8 \times 8 \times 8$  grid. Although the Orlova *et al.* [2014] hiss model using CRRES data was a quadratic function, initial analysis of the RBSP A data suggested that a cubic model would be more appropriate specifically to capture the variation of wave intensity with  $L$ . We apply multiple linear regression to fit the logarithm of  $\langle B_w^2 \rangle$  to a polynomial of order up to 3. Including interaction terms in all four variables ( $K_p$ ,  $L$ ,  $\lambda$ , and MLT), the model can have up to 35 terms. We use a stepwise fitting algorithm in order to include only the most statistically significant terms. Further, the algorithm takes as an input observation weights, and for this we use the square root of the number of points that were averaged in each bin. In this way, the bins with more measurements in the average (for example, low  $K_p$  and low  $\lambda$ ) are weighted higher when performing the fit than bins with few measurements in the average (for example, high  $K_p$  and high  $\lambda$ ). The output of the regression algorithm is a model with 28 terms and has a coefficient of determination ( $R^2$ ) of 0.60 and root-mean-square error of 0.37. The weights for the regression model are provided in the supporting information.



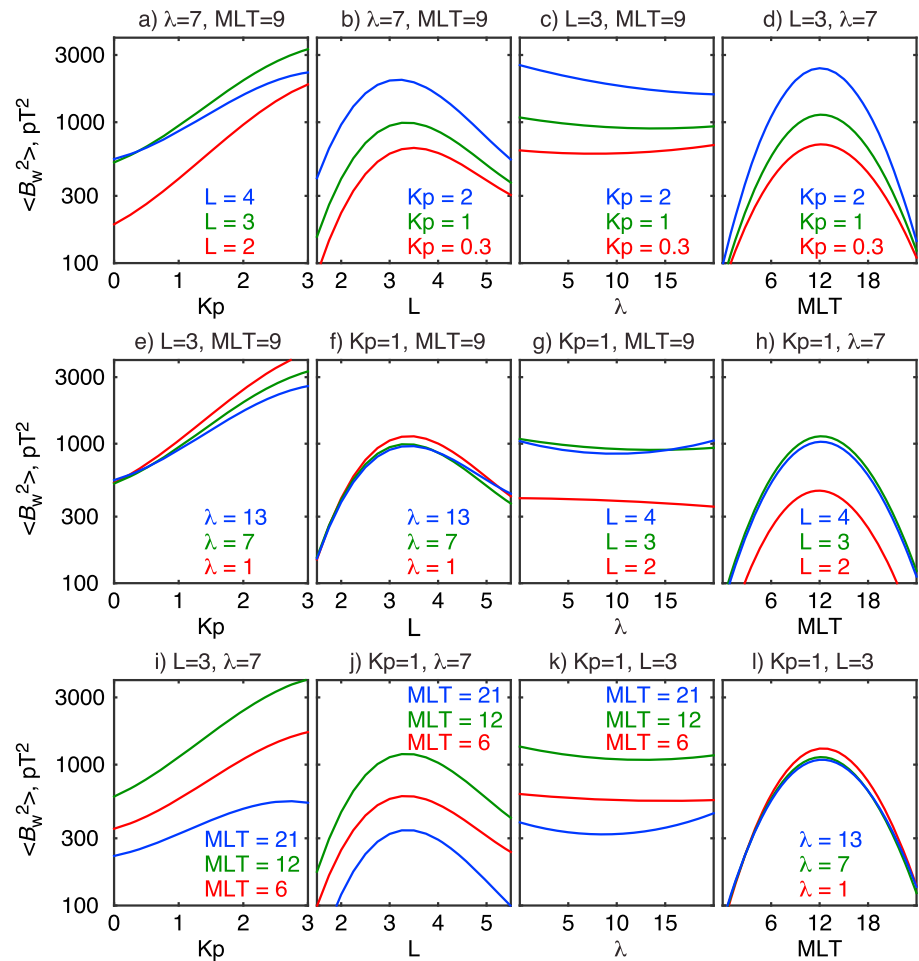


**Figure 6.** Output of the cubic regression model examining the variation of  $\langle B_w^2 \rangle$  as a function of one variable ((a, e, i)  $Kp$ , (b, f, j)  $L$ , (c, g, k)  $\lambda$ , and (d, h, l)  $\text{MLT}$ ) for three values of a second variable (red, green, and blue curves) at fixed values of the third and fourth variables (as indicated in the title of each panel).

One of the main goals of creating the regression model is to explore the overall trends of hiss intensity. Magnetospheric wave data, in general, tend to have a high degree of variance so it can be difficult to visualize the data and determine the most important dependencies. By applying the regression analysis, we can smooth the variance in the four-dimensional bin-averaged data set and plot the output of the model to examine the most relevant trends and the relationships between the four input variables. Figure 6 shows one-dimensional outputs of the regression model with each panel examining the relationship between two input variables. For example, Figure 6a plots  $\langle B_w^2 \rangle$  as a function of  $Kp$  for three values of  $L$  ( $L = 2$  in red,  $L = 3$  in green, and  $L = 4$  in blue) at fixed values of  $\lambda = 7^\circ$  and  $\text{MLT} = 9$  h. Similarly, we explore all ordered pairwise combinations of the input variables with Figures 6a, 6e, and 6i showing the  $Kp$  dependency for different values of  $L$ ,  $\lambda$ , and  $\text{MLT}$ , Figures 6b, 6f, and 6j showing  $L$ , Figures 6c, 6g, and 6k showing  $\lambda$ , and Figures 6d, 6h, and 6l showing  $\text{MLT}$  dependencies.

In examining Figure 6, one trend that becomes apparent is the lack of strong dependence of  $\langle B_w^2 \rangle$  on  $\lambda$  and lack of significant interaction between  $\lambda$  and the other variables. This can be seen in Figures 6c, 6g, and 6k where the variations with  $\lambda$  for various values of  $Kp$ ,  $L$ , and  $\text{MLT}$  are relatively flat compared with trends in other variables. Further, in plots as a function of (Figure 6e)  $Kp$ , (Figure 6f)  $L$ , and (Figure 6l)  $\text{MLT}$ , the curves for the three values of  $\lambda$  essentially lie on top of one another. The lack of  $\lambda$  dependence in the RBSP A data was also noted in the comparison with CRRES data in Figures 4e and 4f.

In terms of  $Kp$ , looking down Figures 6a, 6e, and 6i, we see that  $\langle B_w^2 \rangle$  increases with increasing  $Kp$ , but the  $Kp$  dependence is not fixed for all values of the other input variables. For example, Figure 6i, the  $Kp$  dependence

is stronger at noon (green line) than on the nightside (blue line). This can also be seen in the complementary plot in Figure 6d, in which there is more separation between the curves in the noon sector than the other local times. In Figure 6a, we see that the  $Kp$  dependency at  $L = 2$  is slightly stronger than for the higher  $L$  values, that is, there is a larger relative change in  $\langle B_w^2 \rangle$  for increasing  $Kp$  at lower  $L$ .

For the  $L$  dependence in Figures 6b, 6f, and 6j, we find that hiss wave intensity peaks in the range of  $L = 3.2$ – $3.5$  and falls off more steeply with decreasing  $L$  and more gradually with increasing  $L$ . Figure 6b shows a tendency for the peak hiss intensity to move to lower  $L$  with increasing  $Kp$ . There does not appear to be much change in the  $L$  dependence with local time as seen in both Figures 6j and 6h.

The MLT dependence in Figures 6d, 6h, and 6i indicates that hiss wave intensity peaks at noon and falls off symmetrically to either side of noon. Prior observations of hiss from the CRRES mission did not have full MLT coverage, so the RBSP A measurements provide advanced understanding of the MLT variation, which may have relevance for understanding the origin of hiss [e.g., Bortnik *et al.*, 2008] and provide a test for existing physics-based models of hiss generation and propagation [Chen *et al.*, 2009, 2012b, 2012c].

To summarize, there does not appear to be a significant dependence of hiss intensity on magnetic latitude in the range of  $\sim 0$ – $20^\circ$ . Hiss intensity increases with increasing  $Kp$ , and the  $Kp$  dependence is stronger on the dayside and slight stronger at lower  $L$ . Hiss intensity peaks near  $L = 3.25$  to  $3.5$  for all local times and falls off steeply toward lower  $L$ . Hiss intensity is strongly peaked at noon and falls off symmetrically to either side of noon.

## 5. Simplified Model of Hiss Intensity

The cubic regression model presented in the previous section can be used in quasi-linear diffusion calculation to determine the scattering rate of electrons due to hiss. The model does contain a large number of terms, but the polynomial form of the equation is straightforward to implement. However, there are several advantages to create a more simplified model. For example, the pitch angle diffusion coefficients scale linearly with  $\langle B_w^2 \rangle$ . Therefore, if we neglect the interaction terms between the input variables, we can calculate the diffusion coefficients as a function of a single variable, for example,  $L$ , and scale the diffusion coefficients based on the relative variation with the other variables, for example,  $Kp$  and MLT. Also, in order to construct the 4-D regression model, we have to bin the data somewhat coarsely into 8 quantile bins in each variable. This specifically limits our ability to capture the variation of hiss intensity at high  $Kp$ . The last quantile bin of  $Kp$  for the full regression model includes all measurements from  $Kp = 2.6$  to  $7.7$  with the most likely value of  $Kp$  in that bin being  $3.2$ . However, if we neglect variations in  $Kp$  with  $L$ ,  $\lambda$ , and MLT, we can use finer binning in  $Kp$  and attempt to parametrize hiss intensity for the full range of observed  $Kp$ .

Therefore, we develop a simplified model of average hiss intensity that takes the general form:

$$\langle B_w^2 \rangle = 10^{f(L)} g(\text{MLT}) h(Kp) \quad (1)$$

where  $f(L)$  is a polynomial that describes the log of the  $L$  variation in picoTeslas squared and  $g(\text{MLT})$  and  $h(Kp)$  are dimensionless scaling factors. We neglect all variation with  $\lambda$ .

To determine  $f(L)$ , we divide all the data into 20 quantile bins of  $L$  and compute  $\langle B_w^2 \rangle$  in each bin as shown by the red curve in Figure 7a. The  $L$  dependence,  $f(L)$ , is fit in the least squares sense as a cubic of the form:

$$f(L) = a_3 L^3 + a_2 L^2 + a_1 L + a_0 \quad (2)$$

and is indicated by the black curve in Figure 7a. The fit is valid from  $L = 1.2$  to  $6.1$ , and the weights,  $a_n$ , are in Table 1.

To determine the MLT scaling factor,  $g(\text{MLT})$ , we first divide the data in the range  $2 < L < 5.5$  into 12 quantile bins of MLT and compute the average as shown by the red curve in Figure 7b. The unscaled MLT dependence,  $g_o(\text{MLT})$ , is fit as a quadratic of the form

$$g_o(\text{MLT}) = b_2 \text{MLT}^2 + b_1 \text{MLT} + b_0 \quad (3)$$

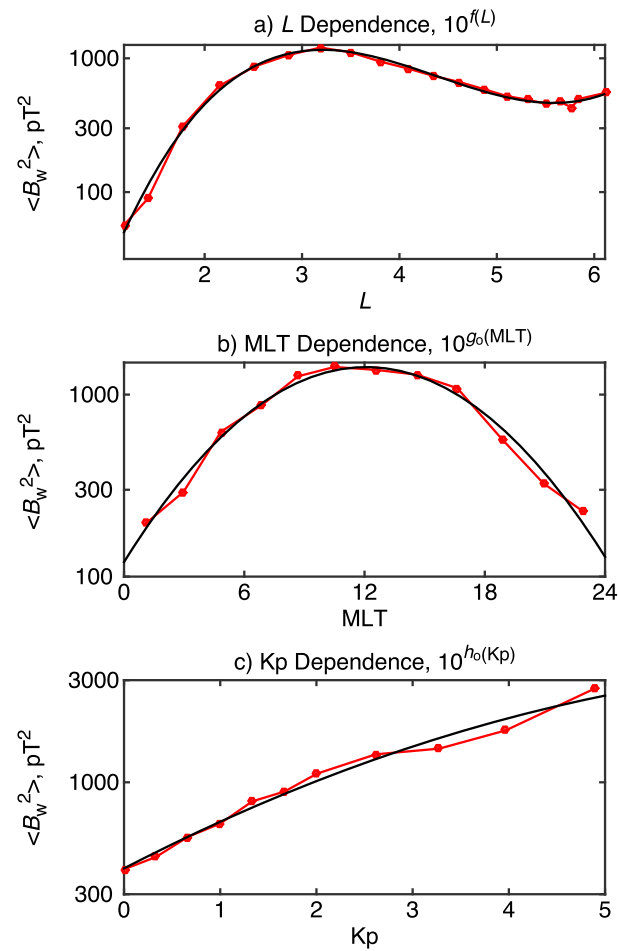


**Figure 7.** (a) Average hiss intensity as a function of  $L$  measured by RBSP A (red) and a cubic fit to the data corresponding to equation (2) (black). (b)  $\langle B_w^2 \rangle$  as a function of MLT measured (red) and a quadratic fit from equation (3) (black). (c)  $\langle B_w^2 \rangle$  as a function of  $Kp$  measured (red) and a quadratic fit from equation (5) (black).

and is indicated by the black curve in Figure 7b with the weights,  $b_n$ , included in Table 1. We obtain the MLT scaling factor,  $g(MLT)$ , as

$$g(MLT) = \frac{1}{G_o} 10^{g_o(MLT)} \quad (4)$$

where  $G_o = \frac{1}{24} \int_0^{24} 10^{g_o(MLT)} dMLT$  with the value of  $G_o$  given in Table 1.

The  $Kp$  scaling factor,  $h(Kp)$ , is determined in an analogous manner except we use 11 manually selected bins to extend the fit to higher values of  $Kp$ . The bin-averaged data are shown by the red curve in Figure 7c where

**Table 1.** Weights for the Simplified Model of  $\langle B_w^2 \rangle$  Described by Equations (1)–(6)

| $f(L)$   | $a_3$   | $a_2$     | $a_1$  | $a_0$  |
|----------|---------|-----------|--------|--------|
|          | 0.05894 | −0.7768   | 3.163  | −1.036 |
| $g(MLT)$ | $G_o$   | $b_2$     | $b_1$  | $b_0$  |
|          | 782.3   | −0.007338 | 0.1773 | 2.080  |
| $h(Kp)$  | $H_o$   | $c_2$     | $c_1$  | $c_0$  |
|          | 1315    | −0.01414  | 0.2321 | 2.598  |

the last bin extends from  $Kp = 4.3$  to  $7.6$  with a median value of  $4.9$  and contains  $1.2\%$  of the total data. The unscaled  $Kp$  dependence,  $h_o(Kp)$ , is fit as a quadratic of the form

$$h_o(Kp) = c_2 Kp^2 + c_1 Kp + c_0 \quad (5)$$

and is indicated by the black curve in Figure 7d. The fit is valid from  $Kp = 0$  to  $5$ , and the weights,  $c_n$ , are in Table 1. The  $Kp$  scaling factor is then

$$h(Kp) = \frac{1}{H_o} 10^{h_o(Kp)} \quad (6)$$

and the value of  $H_o$  is given in Table 1.

Note that we repeated the above analysis restricting the data in magnetic latitude as  $>3^\circ$ ,  $>5^\circ$ , and  $<5^\circ$ . This was done in order to examine any possible contribution of equatorially confined emissions, particularly with increasing levels of  $Kp$ . In all three latitude regimes, we find that the curves lie essentially on top of the curves in Figure 7, and we conclude that equatorially confined emissions are not a significant contribution to the wave model.

## 6. Summary

The Van Allen Probes mission provides comprehensive coverage of the plasma wave environment in the inner magnetosphere. Using 2 years of data from the RBSP A satellite, we constructed a database of plasmaspheric hiss observations taking advantage of the routine three-channel measurements from the EMFISIS instrument, which provide for a more accurate calculation of the total wave magnetic field, and improved low-frequency response. Past studies of electron lifetimes due to scattering from hiss have extensively used measurements from the CRRES spacecraft, and we performed detailed comparisons of the two databases. Compared with CRRES, RBSP A provides improved coverage at lower  $L$ , for application to the slot region and inner belt, and improved coverage on the dayside where hiss tends to be most intense. On the other hand, the CRRES mission occurred during a stronger period of geomagnetic activity and provides measurements that extend to higher latitude. After performing comparisons of the integrated wave amplitude for regions of spatial and geomagnetic overlap, we find that the CRRES measurements of hiss wave electric field amplitude are in reasonable agreement with RBSP A electric field measurements. However, when comparing the CRRES inferred magnetic field with the RBSP A measured magnetic field, we find that the assumptions that go into the CRRES  $E$  to  $B$  conversion result in an overestimation of the total wave magnetic field and a latitudinal dependence that is inconsistent with findings from RBSP A.

We developed two empirical models of the average hiss magnetic field intensity,  $\langle B_w^2 \rangle$  using RBSP A data. The first is a regression model that contains 28 terms of up to third order in  $Kp$ ,  $L$ ,  $\lambda$ , and MLT. The coefficients are provided in the supporting information, and the model is valid for  $0 \leq Kp \leq 3.2$ ,  $1.8 \leq L \leq 5.4$ ,  $0 \leq |\lambda| \leq 20^\circ$ , and  $0 \leq \text{MLT} \leq 24$ . We also present a simplified model of  $\langle B_w^2 \rangle$  that neglects any latitudinal dependence and neglects interactions between  $Kp$ ,  $L$ , and MLT. The model is presented in equations (1)–(6) and Table 1. A key advantage of the simplified model is the ability to parametrize over a wider range of  $Kp$ , and lack of cross terms provides some advantages for scaling of the diffusion coefficients. The simplified model is valid for  $0 \leq Kp \leq 5$ ,  $1.2 \leq L \leq 6.1$ , and  $0 \leq \text{MLT} \leq 24$  and can be applied for  $0 \leq |\lambda| \leq 20^\circ$ . The models provide the hiss intensity as a continuous function of the input variables, and the simplified model provides parametrization over a wider range of geomagnetic conditions than previous models. We believe that the use of these new empirical models in quasi-linear diffusion calculations will improve the accuracy of electron diffusion rates and lifetimes due to scattering by hiss.

The statistical analysis of hiss presented here allows us to make the following conclusions about the global distribution and variation of plasmaspheric hiss:

1. Hiss intensity increases with increasing  $Kp$ , and there is no evidence of the saturation of hiss amplitudes for  $Kp$  up to  $5$ .
2. Hiss intensity peaks near  $L = 3.25$  to  $3.5$  for all local times, and the intensity falls off steeply toward lower  $L$  and more gradually to higher  $L$ . Lower  $L$  values tend to have a slightly stronger  $Kp$  dependence, that is, the relative amplitude increase for increasing  $Kp$  is greater near  $L = 2$ .

3. In the range of  $|\lambda| = 0-20^\circ$ , there does not appear to be a significant dependence of hiss intensity on magnetic latitude in contrast to previous analysis using CRRES inferred magnetic field data.
4. Hiss intensity peaks at 12 MLT and falls off symmetrically to either side of noon. The local time peak of hiss does not appear to vary with  $K_p$  or  $L$ . The dayside has a stronger  $K_p$  dependence than the nightside.

# Acknowledgments

The work at Stanford University was supported under NASA awards NNX14AC04G and NNX15AI94G. Y.Y.S. acknowledges support from NASA awards NNX10AK99G and NNX13AE34G, NSF award AGS-1243183, UC Lab Fee award 116720, and Horizon 2020 award 637302. All Van Allen Probes data were accessed through the EMFISIS website hosted at the University of Iowa, and we graciously thank the EMFISIS Principal Investigator, Craig Kletzing, and the EMFISIS team. The  $K_p$  index was provided by the World Data Center. Other data sets used in this study can be accessed by contacting the first author.

# References

- Abel, B., and R. M. Thorne (1998), Electron scattering loss in Earth's inner magnetosphere 1. Dominant physical processes, *J. Geophys. Res.*, **103**, 2385–2396, doi:10.1029/97JA02919.
- Agapitov, O., A. Artemyev, V. Krasnoselskikh, Y. V. Khotyaintsev, D. Mourenas, H. Breuillard, M. Balikhin, and G. Rolland (2013), Statistics of whistler mode waves in the outer radiation belt: Cluster STAFF-SA measurements, *J. Geophys. Res. Space Physics*, **118**, 3407–3420, doi:10.1002/jgra.50312.
- Agapitov, O. V., A. V. Artemyev, D. Mourenas, Y. Kasahara, and V. Krasnoselskikh (2014), Inner belt and slot region electron lifetimes and energization rates based on Akebono statistics of whistler waves, *J. Geophys. Res. Space Physics*, **119**, 2876–2893, doi:10.1002/2014JA019886.
- Albert, J. M. (2000), Pitch angle diffusion as seen by CRRES, *Adv. Space Res.*, **25**, 2343–2346, doi:10.1016/S0273-1177(99)00520-7.
- Anderson, B. J., R. E. Erlandson, and L. J. Zanetti (1992), A statistical study of Pc 1–2 magnetic pulsations in the equatorial magnetosphere: 1. Equatorial occurrence distributions, *J. Geophys. Res.*, **97**, 3075–3088, doi:10.1029/91JA02706.
- Bortnik, J., R. M. Thorne, and N. P. Meredith (2008), The unexpected origin of plasmaspheric hiss from discrete chorus emissions, *Nature*, **452**, 62–66, doi:10.1038/nature06741.
- Bortnik, J., R. M. Thorne, and N. P. Meredith (2009), Plasmaspheric hiss overview and relation to chorus, *J. Atmos. Sol. Terr. Phys.*, **71**, 1636–1646, doi:10.1016/j.jastp.2009.03.023.
- Bortnik, J., L. Chen, W. Li, R. M. Thorne, and R. B. Horne (2011), Modeling the evolution of chorus waves into plasmaspheric hiss, *J. Geophys. Res.*, **116**, A08221, doi:10.1029/2011JA016499.
- Chen, L., J. Bortnik, R. M. Thorne, R. B. Horne, and V. K. Jordanova (2009), Three-dimensional ray tracing of VLF waves in a magnetospheric environment containing a plasmaspheric plume, *Geophys. Res. Lett.*, **36**, L22101, doi:10.1029/2009GL040451.
- Chen, L., W. Li, J. Bortnik, and R. M. Thorne (2012a), Amplification of whistler-mode hiss inside the plasmasphere, *Geophys. Res. Lett.*, **39**, L08111, doi:10.1029/2012GL051488.
- Chen, L., J. Bortnik, W. Li, R. M. Thorne, and R. B. Horne (2012b), Modeling the properties of plasmaspheric hiss: 1. Dependence on chorus wave emission, *J. Geophys. Res.*, **117**, A05201, doi:10.1029/2011JA017201.
- Chen, L., J. Bortnik, W. Li, R. M. Thorne, and R. B. Horne (2012c), Modeling the properties of plasmaspheric hiss: 2. Dependence on the plasma density distribution, *J. Geophys. Res.*, **117**, A05202, doi:10.1029/2011JA017202.
- Golden, D. I., M. Spasojevic, W. Li, and Y. Nishimura (2012), Statistical modeling of plasmaspheric hiss amplitude using solar wind measurements and geomagnetic indices, *Geophys. Res. Lett.*, **39**, L06103, doi:10.1029/2012GL051185.
- Green, J. L., S. Boardsen, L. Garcia, W. W. L. Taylor, S. F. Fung, and B. W. Reinisch (2005), On the origin of whistler mode radiation in the plasmasphere, *J. Geophys. Res.*, **110**, A03201, doi:10.1029/2004JA010495.
- Gurnett, D. A., and T. B. Burns (1968), The low-frequency cutoff of ELF emissions, *J. Geophys. Res.*, **73**, 7437–7445, doi:10.1029/JA073i023p07437.
- Hayakawa, M., and S. S. Sazhin (1992), Mid-latitude and plasmaspheric hiss—A review, *Planet. Space Sci.*, **40**, 1325–1338, doi:10.1016/0032-0633(92)90089-7.
- Kennel, C. F., and F. Engelmann (1966), Velocity space diffusion from weak plasma turbulence in a magnetic field, *Phys. Fluids*, **9**, 2377, doi:10.1063/1.1761629.
- Kim, K.-C., D.-Y. Lee, and Y. Shprits (2015), Dependence of plasmaspheric hiss on solar wind parameters and geomagnetic activity and modeling of its global distribution, *J. Geophys. Res. Space Physics*, **120**, 1153–1167, doi:10.1002/2014JA020687.
- Kletzing, C. A., et al. (2013), The Electric and Magnetic Field Instrument Suite and Integrated Science (EMFISIS) on RBSP, *Space Sci. Rev.*, **179**, 127–181, doi:10.1007/s11214-013-9993-6.
- Kurth, W. S., S. D. Pascuale, J. B. Faden, C. A. Kletzing, G. B. Hospodarsky, S. Thaller, and J. R. Wygant (2015), Electron densities inferred from plasma wave spectra obtained by the waves instrument on Van Allen Probes, *J. Geophys. Res. Space Physics*, **120**, 904–914, doi:10.1002/2014JA020857.
- Lam, M. M., R. B. Horne, N. P. Meredith, and S. A. Glauert (2007), Modeling the effects of radial diffusion and plasmaspheric hiss on outer radiation belt electrons, *Geophys. Res. Lett.*, **34**, L20112, doi:10.1029/2007GL031598.
- Ledocq, M. J., D. A. Gurnett, and R. R. Anderson (1994), Electron number density fluctuations near the plasmopause observed by the CRRES spacecraft, *J. Geophys. Res.*, **99**, 23,661–23,671, doi:10.1029/94JA02294.
- Li, W., Y. Y. Shprits, and R. M. Thorne (2007), Dynamic evolution of energetic outer zone electrons due to wave-particle interactions during storms, *J. Geophys. Res.*, **112**, A10220, doi:10.1029/2007JA012368.
- Li, W., et al. (2013), An unusual enhancement of low-frequency plasmaspheric hiss in the outer plasmasphere associated with substorm-injected electrons, *Geophys. Res. Lett.*, **40**, 3798–3803, doi:10.1002/grl.50787.
- Li, W., Q. Ma, R. M. Thorne, J. Bortnik, C. A. Kletzing, W. S. Kurth, G. B. Hospodarsky, and Y. Nishimura (2015), Statistical properties of plasmaspheric hiss derived from Van Allen Probes data and their effects on radiation belt electron dynamics, *J. Geophys. Res. Space Physics*, **120**, 3393–3405, doi:10.1002/2015JA021048.
- Lyons, L. R., and R. M. Thorne (1972), Parasitic pitch angle diffusion of radiation belt particles by ion cyclotron waves, *J. Geophys. Res.*, **77**, 5608–5616, doi:10.1029/JA077i028p05608.
- Lyons, L. R., and R. M. Thorne (1973), Equilibrium structure of radiation belt electrons, *J. Geophys. Res.*, **78**, 2142–2149, doi:10.1029/JA078i013p02142.
- Mauk, B. H., N. J. Fox, S. G. Kanekal, R. L. Kessel, D. G. Sibeck, and A. Ukhorskiy (2012), Science objectives and rationale for the Radiation Belt Storm Probes mission, *Space Sci. Rev.*, **179**, 3–27, doi:10.1007/s11214-012-9908-y.
- Meredith, N. P., R. B. Horne, R. M. Thorne, D. Summers, and R. R. Anderson (2004), Substorm dependence of plasmaspheric hiss, *J. Geophys. Res.*, **109**, A06209, doi:10.1029/2004JA010387.
- Meredith, N. P., R. B. Horne, M. A. Clilverd, D. Horsfall, R. M. Thorne, and R. R. Anderson (2006a), Origins of plasmaspheric hiss, *J. Geophys. Res.*, **111**, A09217, doi:10.1029/2006JA011707.
- Meredith, N. P., R. B. Horne, S. A. Glauert, R. M. Thorne, D. Summers, J. M. Albert, and R. R. Anderson (2006b), Energetic outer zone electron loss timescales during low geomagnetic activity, *J. Geophys. Res.*, **111**, A05212, doi:10.1029/2005JA011516.



- Meredith, N. P., R. B. Horne, S. A. Glauert, and R. R. Anderson (2007), Slot region electron loss timescales due to plasmaspheric hiss and lightning-generated whistlers, *J. Geophys. Res.*, *112*, A08214, doi:10.1029/2007JA012413.
- Meredith, N. P., R. B. Horne, S. A. Glauert, D. N. Baker, S. G. Kanekal, and J. M. Albert (2009), Relativistic electron loss timescales in the slot region, *J. Geophys. Res.*, *114*, A03222, doi:10.1029/2008JA013889.
- Millan, R. M., and R. M. Thorne (2007), Review of radiation belt relativistic electron losses, *J. Atmos. Sol. Terr. Phys.*, *69*, 362–377, doi:10.1016/j.jastp.2006.06.019.
- Mosier, S. R., M. L. Kaiser, and L. W. Brown (1973), Observations of noise bands associated with the upper hybrid resonance by the IMP 6 radio astronomy experiment, *J. Geophys. Res.*, *78*, 1673–1679, doi:10.1029/JA078i010p01673.
- Ni, B., R. M. Thorne, N. P. Meredith, Y. Y. Shprits, and R. B. Horne (2011), Diffuse auroral scattering by whistler mode chorus waves: Dependence on wave normal angle distribution, *J. Geophys. Res.*, *116*, A10207, doi:10.1029/2011JA016517.
- Orlova, K., M. Spasojevic, and Y. Shprits (2014), Activity-dependent global model of electron loss inside the plasmasphere, *Geophys. Res. Lett.*, *41*, 3744–3751, doi:10.1002/2014GL060100.
- Selesnick, R. S., J. B. Blake, and R. A. Mewaldt (2003), Atmospheric losses of radiation belt electrons, *J. Geophys. Res.*, *108*, 1468, doi:10.1029/2003JA010160.
- Shprits, Y. Y., D. A. Subbotin, N. P. Meredith, and S. R. Elkington (2008), Review of modeling of losses and sources of relativistic electrons in the outer radiation belt II: Local acceleration and loss, *J. Atmos. Sol. Terr. Phys.*, *70*, 1694–1713, doi:10.1016/j.jastp.2008.06.014.
- Shprits, Y. Y., D. Subbotin, and B. Ni (2009), Evolution of electron fluxes in the outer radiation belt computed with the verb code, *J. Geophys. Res.*, *114*, A11209, doi:10.1029/2008JA013784.
- Shprits, Y. Y., D. Subbotin, A. Drozdov, M. E. Usanova, A. Kellerman, K. Orlova, D. N. Baker, D. L. Turner, and K.-C. Kim (2013), Unusual stable trapping of the ultrarelativistic electrons in the Van Allen radiation belts, *Nat. Phys.*, *9*, 699–703, doi:10.1038/nphys2760.
- Singer, H. J., W. P. Sullivan, P. Anderson, F. Mozer, P. Harvey, J. Wygant, and W. McNeil (1992), Fluxgate magnetometer instrument on the CRRES, *J. Spacecr. Rockets*, *29*, 599–601, doi:10.2514/3.25506.
- Smith, R. L., and N. Brice (1964), Propagation in multicomponent plasmas, *J. Geophys. Res.*, *69*, 5029–5040, doi:10.1029/JZ069i023p05029.
- Sonwalkar, V. S., and U. S. Inan (1989), Lightning as an embryonic source of VLF hiss, *J. Geophys. Res.*, *94*, 6986–6994, doi:10.1029/JA094iA06p06986.
- Summers, D., B. Ni, and N. P. Meredith (2007), Timescales for radiation belt electron acceleration and loss due to resonant wave-particle interactions: 2. Evaluation for VLF chorus, ELF hiss, and electromagnetic ion cyclotron waves, *J. Geophys. Res.*, *112*, A04207, doi:10.1029/2006JA011993.
- Thorne, R. M., S. R. Church, and D. J. Gorney (1979), On the origin of plasmaspheric hiss—The importance of wave propagation and the plasmopause, *J. Geophys. Res.*, *84*, 5241–5247, doi:10.1029/JA084iA09p05241.
- Thorne, R. M., et al. (2013), Evolution and slow decay of an unusual narrow ring of relativistic electrons near  $L \sim 3.2$  following the September 2012 magnetic storm, *Geophys. Res. Lett.*, *40*, 3507–3511, doi:10.1002/grl.50627.
- Tsurutani, B. T., B. J. Falkowski, J. S. Pickett, O. Santolik, and G. S. Lakhina (2015), Plasmaspheric hiss properties: Observations from Polar, *J. Geophys. Res. Space Physics*, *120*, 414–431, doi:10.1002/2014JA020518.
- Wygant, J. R., et al. (2013), The electric field and waves instruments on the Radiation Belt Storm Probes mission, *Space Sci. Rev.*, *179*, 183–220, doi:10.1007/s11214-013-0013-7.